




Investigating fusion attributes in $^{30}\text{Si}+^{140}\text{Ce}$ reaction around the barrier

Malvika Sagwal¹, Moumita Maiti^{1,a} , Rishabh Kumar¹, Pavneet Kaur¹, Ankur Singh¹, Himanshu Sharma¹, Yasir Arafat¹, Chandra Kumar², Gonika², J. Gehlot², S. Nath², N. Madhavan²

¹ Department of Physics, Indian Institute of Technology Roorkee, Roorkee, Uttarakhand 247667, India

² Nuclear Physics Group, Inter-University Accelerator Centre, New Delhi 110067, India

Received: 3 April 2024 / Accepted: 6 August 2024

© The Author(s), under exclusive licence to Società Italiana di Fisica and Springer-Verlag GmbH Germany, part of Springer Nature 2024

Communicated by Alessia Di Pietro

Abstract In heavy-ion collision experiments, the fusion cross section in the sub-barrier energy region is found to be enhanced by several orders of magnitude in comparison to the prediction of the one-dimensional barrier penetration model (1D-BPM) that involves the quantum mechanical tunneling effect during fusion. So far, the coupling-aided tunneling due to participating nuclei's intrinsic degrees of freedom continues to be identified as an accountable factor. We intend to probe the role of structural properties and low-lying inelastic excitations of the colliding nuclei in driving the fusion phenomenon for energies in the near and sub-barrier regions. In the study, the fusion excitation function has been measured for $^{30}\text{Si}+^{140}\text{Ce}$ reaction for energies $\approx 11\%$ below to 13% above the Coulomb barrier. The measured fusion cross section is found to be noticeably enhanced in the sub-barrier region compared to the corresponding 1D-BPM prediction. The coupled-channel (CC) formalism in the CCFULL framework has been employed to interpret the aforementioned intricate processes involved in fusion. The present results have been compared with those of a few nearby mass systems to understand different aspects of channel coupling in heavy-ion fusion.

1 Introduction

The growing interest in heavy-ion ($A > 4$) fusion dynamics has led to new experiments in near Coulomb barrier, sub-barrier, and deep sub-barrier energy regions. The fusion phenomenon in the nuclear collision was *prima facie* expected to happen at incident projectile energies above the Coulomb barrier. However, it has been seen to extend to even lower bombarding energies against our classical intuition, possibly

due to the quantum mechanical tunneling phenomenon in the dinuclear system. Furthermore, in heavier systems, fusion cross sections are enhanced by multiple orders of magnitude compared to the predictions of the standard one-dimensional barrier penetration model (1D-BPM) [1–4] for fusion in the sub-barrier energy region. Theoretical examination of these striking observations puts forth the role of couplings to various intrinsic degrees of freedom of the projectile and target nuclei and manifests the splitting of a single barrier into multiple [5].

Initial studies by Stokstad et al. and Beckerman et al. [1–3] on $^{16}\text{O}+^{148,150,152,154}\text{Sm}$ and $^{58}\text{Ni}+^{58}\text{Ni}$, systems, respectively, link this substantial fusion enhancement below the barrier with structural effects of participating nuclei. Analytical models within coupled-channel (CC) formalism [6], including different degrees of freedom of the projectile-target nuclei [7], e.g., inelastic excitations among vibrational and rotational states [8–20], static deformation [3, 16, 17, 20–22], and nucleon transfer [13, 14, 17, 18, 23–25] are applied to understand the fusion data exhaustively. While the role of collective excitations of vibrational and rotational states is unambiguously found to be strong on a general level, the extent to which various couplings contribute varies in studies.

For instance, in the case of $^{32}\text{S}+^{112,116,120}\text{Sn}$, Tripathi et al. [8] noted that there is a dominant role of the couplings to surface vibrations with the multiple phonon excitation of the lowest 2^+ and 3^- states of Sn, 2^+ state of the ^{32}S . The transfer effects inevitably interplay with nuclear structural effects in disentangling couplings related to the fusion [10]. The systems, e.g., $^{40}\text{Ca}+^{90,96}\text{Zr}$ [13, 26] had been chosen to examine the influence of multi-phonon octupole vibration, which is stronger and lower in energy in ^{96}Zr compared to ^{90}Zr . $^{40}\text{Ca}+^{96}\text{Zr}$ has positive Q-value neutron transfer (PQNT) channels at the same time. To precisely solve this problem, some later studies were done using $^{48}\text{Ca}+^{90,94,96}\text{Zr}$ [9–11],

^a e-mail: moumita.maiti@ph.iitr.ac.in (corresponding author)

with no transfer channel. It was observed that there is a less pronounced effect of this octupole state of ^{96}Zr , and hence the fusion enhancement was attributed to mainly neutron transfer channels for the previous system $^{40}\text{Ca}+^{96}\text{Zr}$.

A more recent experiment on $^{28}\text{Si}+^{116,120,124}\text{Sn}$ systems [14] suggests that the inclusion of the structural effect of oblate-deformed rotational ^{28}Si and spherical (vibrational) Sn with correct transfer strength in theoretical models is essential to justify the data. Several deformed nuclei exhibiting rotational structure carry inelastic excitations to low-lying states during fusion, e.g., 0^+ , 2^+ , 4^+ , and so on, and therefore, aid channel coupling. Similarly, in $^{28,30}\text{Si}+^{158,156}\text{Gd}$ systems, the sensitivity of different inelastic excitations in ^{28}Si , ^{30}Si , and Gd along with transfer channels of the colliding nuclei are reported in Ref. [19,24]. These experimentally measured excitation functions were analyzed in the framework of CC formalism using the CCFULL [27] and ECC [28] programs. It signifies that accurately treating the transfer channels and collective excitations is imperative to achieve a good agreement with the measured fusion data [14,17,18].

Additionally, the nature of fusion barrier distribution [5,29,30] has been discussed thoroughly within the realm of CC calculations for many systems [8,16,19,20,31]. From the study of substantial fusion data available, it becomes more or less clear that couplings have a direct influence on the collective excitations of the colliding partners in the sub-barrier fusion enhancement. However, more high-precision data and analysis are required to unambiguously pinpoint the role of structural peculiarities of the involved nuclei.

Carrying this motivation, the present report focuses on $^{30}\text{Si}+^{140}\text{Ce}$ reaction study through the fusion excitation function measurement for energies spanning $\approx 11\%$ below to 13% above the Coulomb barrier. ^{30}Si is a deformed nucleus with $\beta_2 = 0.315$, while ^{140}Ce is a nearly spherical nucleus having a neutron shell closed structure ($N = 82$). Both nuclei exhibit vibrational excitations. We aim to investigate the role of structural degrees of freedom, i.e., deformation and inelastic excitations of nuclei, on the sub-barrier fusion through CC calculations. The absence of any positive Q-value corresponding to nucleon transfer reduces the complications in inferring the outcomes of the channel-coupling effect of the nuclei involved. Hence, the goal is to analyze the relative influence of these structural features on the fusion phenomenon through a systematic comparison with available studies based on nearby mass systems. The organization of this article is as follows: Sect. 2 presents the experimental procedure; Sect. 3 discusses the data analysis, results, and theoretical interpretations. Eventually, Sect. 4 concludes the report.

2 Experimental details

The fusion measurement was performed at the 15 UD Pelletron accelerator facility of the Inter-University Accelerator Centre (IUAC), New Delhi. A pulsed beam of ^{30}Si was used to bombard the $200\ \mu\text{g}/\text{cm}^2$ thick ^{140}Ce target (99.72% enrichment) with $20\ \mu\text{g}/\text{cm}^2$ carbon backing. The target was prepared using the physical vapor deposition technique [32]. It was kept in the target chamber in a way that carbon backing faced the beam. Two Passivated Implanted Planar Silicon (PIPS) detectors, M_L and M_R with 0.5 mm entrance aperture were placed inside the chamber at $\theta_{lab} = 26.1^\circ$ relative to the beam direction. The elastically scattered beam particles recorded by the PIPS detectors were used for the absolute normalization of the evaporation residue (ER) cross section. Secondly, using the PIPS detectors and beam current maximization at the catcher (Faraday cup), the beam was positioned at the center of the target (Fig. 1).

The ERs produced in the reaction were segregated from the enormous beam background and transported to the focal plane detector by the HYbrid Recoil mass Analyzer (HYRA) [33,34] shown in Fig. 1. It is a dual-mode, dual-stage recoil mass separator and spectrometer. When used as a gas-filled separator, the first stage is operated in the momentum dispersive mode for normal kinematics. Together, both stages can act as momentum achromats in the vacuum mode of operation for inverse kinematics. Only the first stage of HYRA with gas-filled mode was used for the present $^{30}\text{Si}+^{140}\text{Ce}$ reaction. The electromagnetic configuration of HYRA, consisting of quadrupole magnets (Qs) and dipole magnets (MDs), is $Q_1 Q_2\text{-MD}_1\text{-Q}_3\text{-MD}_2\text{-Q}_4 Q_5$.

Gas-filled separators provide better transmission than vacuum-mode separators due to their inherent velocity and

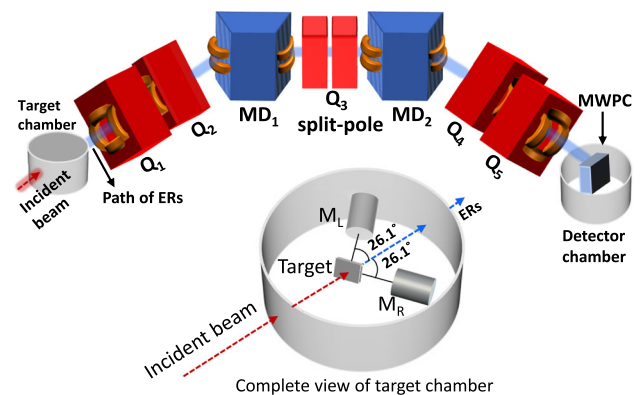


Fig. 1 The schematic diagram of the first stage of HYbrid Recoil mass Analyzer (HYRA). Q and MD indicate the magnetic quadrupoles and magnetic dipoles, respectively. A detailed view of the target chamber has also been given

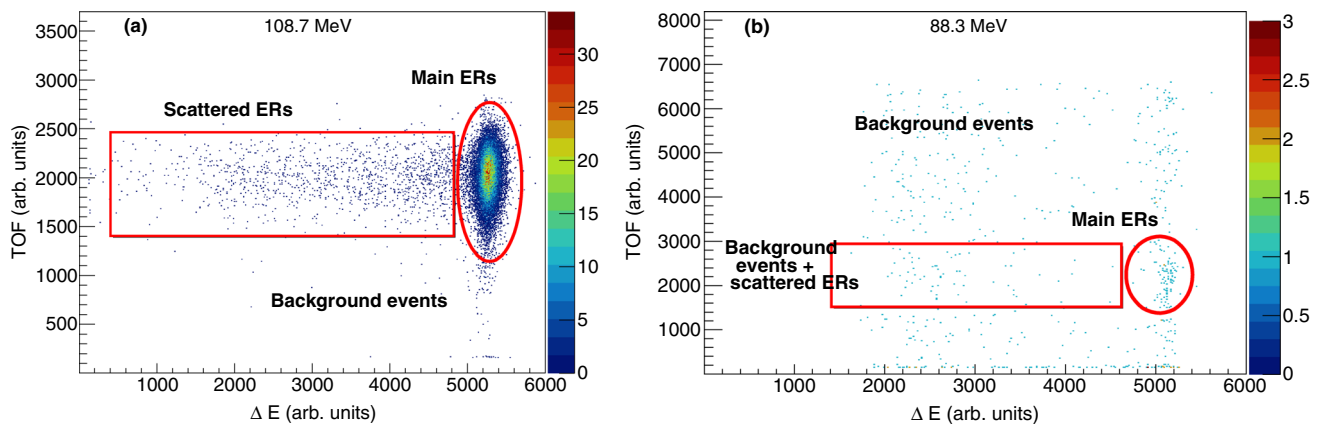


Fig. 2 Two-dimensional plots of energy loss (ΔE) vs. time-of-flight (TOF) of the ERs from $^{30}\text{Si}+^{140}\text{Ce}$ reaction along with beam background at (a) $E_{c.m.} = 108.7$ MeV, and (b) $E_{c.m.} = 88.3$ MeV. The ERs are marked on both panels

charge-state focusing. The helium gas molecules cause multiple collisions with the ERs, changing their energies, charge states, and angles. Owing to the optimum settings of gas pressure and magnetic field values, the ERs follow a mean trajectory defined by the mean charge state attained. The gas pressure in HYRA was scanned and set for the maximum transmission of ERs to the focal plane detector. The optimum gas pressure value was found to be 0.21 Torr. The field values of the magnets and mean charge state were calculated using a simulation code developed in-house [35]. To empirically determine the best field settings at each value of the projectile energy, the field values were varied within $\pm 10\%$ of the calculated values, keeping the gas pressure unchanged. The spectrometer offers a primary beam rejection factor of 10^{12} in the gas-filled mode [33]. A carbon pressure-window foil of $650 \mu\text{g}/\text{cm}^2$ was fixed at the entrance of the target chamber to segregate the beam-line vacuum from the gas-filled region of the separator. The ER measurement was done at $E_{c.m.} = 86.6\text{--}108.7$ MeV ($E_{lab} = 105.2\text{--}132.0$ MeV) after correcting the loss in pressure-window foil, carbon backing, and half-target thickness using the SRIM software [36]. The Coulomb barrier of the system is 96.73 MeV [37] in the center-of-mass frame. The beam energy was varied between $\approx 11\%$ below to 13% above the Coulomb barrier.

The low-energy ERs were detected by the multi-wire proportional counter (MWPC) with an active area of 15.0×5.0 cm^2 , placed at the focal plane of HYRA. The MWPC was operated with isobutane gas at 2.5 Torr pressure and was separated from the HYRA gas-filled region by a mylar foil of $0.5 \mu\text{m}$ thickness. The detector provided the position signal, energy loss (ΔE) signal from the cathode, and timing signal from the anode. The four position signals (two horizontal and two vertical) were taken from the MWPC, followed by delay-line chips. Master trigger was generated for the data acquisition system through the logical OR signal of monitors and the MWPC anode. The time-of-flight (TOF) signal

was acquired through a time-to-amplitude converter (TAC), where the MWPC anode signal acted as a start and suitably delayed radio-frequency (rf) signal as a stop signal. The beam pulse separation was kept at $2 \mu\text{s}$ at low energies to remove ambiguities in identifying ERs. However, it was kept at $1 \mu\text{s}$ to compensate for the low beam current at the highest three energies. TOF information assisted in distinctly identifying the beam-like particles and the ERs. Figure 2 shows the two-dimensional plot of ΔE vs. TOF. Blank runs were taken at low energies to confirm the identification of the ERs. The VME-based data acquisition system was incorporated. The data were collected using IUAC software NIAS-MARS [38] and analyzed using the ROOT framework.

3 Results and discussion

3.1 Data analysis

As the PACE4 [39] predicted fission cross section is negligible for the present system in the measured energy region, the fusion phenomenon should result solely in ER production, i.e., $\sigma_{fus} = \sigma_{ER}$. Post measurement, the absolute ER cross section was estimated using the following relation:

$$\sigma_{ER} = \frac{Y_{ER}}{Y_{mon}} \left(\frac{d\sigma}{d\Omega} \right)_R \Omega_{mon} \frac{1}{\epsilon_{HYRA}} \quad (1)$$

where the σ_{ER} , Y_{ER} , and Y_{mon} represent the measured ER cross section in mb, the ER yield at the focal plane of MWPC, and the geometric mean of the yields measured by the left and right monitor (PIPS), respectively. Ω_{mon} is the solid angle subtended by the monitor detector at the target center, and ϵ_{HYRA} is the transmission efficiency of HYRA. $(\frac{d\sigma}{d\Omega})_R$ is the differential Rutherford scattering cross section in the labora-

tory system. In the cross section calculation, the ϵ_{HYRA} is a crucial factor, given by the following relation:

$$\epsilon_{HYRA} = \frac{\text{Number of ERs reaching the focal plane of HYRA}}{\text{Total number of ERs produced in the reaction}} \quad (2)$$

ϵ_{HYRA} depends on several parameters such as beam energy, entrance-channel mass asymmetry, exit channel of interest, target thickness, angular acceptance of HYRA, size of the focal plane, magnetic field strengths, and the helium gas pressure settings of HYRA. In the $^{30}\text{Si}+^{140}\text{Ce}$ reaction study, the angular acceptance of HYRA, entrance-channel mass asymmetry, target thickness, and the size of the focal plane of MWPC were fixed.

To estimate ϵ_{HYRA} , an experimental reference has been taken from $^{32}\text{S}+^{138}\text{Ba}$ reaction [40] that forms the same compound nucleus $^{170}\text{Hf}^*$ as $^{30}\text{Si}+^{140}\text{Ce}$ reaction. The fusion cross sections for this calibration reaction ($^{32}\text{S}+^{138}\text{Ba}$) were available in the literature [40]. We have measured ERs from both reactions, i.e., $^{32}\text{S}+^{138}\text{Ba}$ and $^{30}\text{Si}+^{140}\text{Ce}$, under the same experimental conditions. The $^{32}\text{S}+^{138}\text{Ba}$ system has been measured at three lab energies, i.e., $E_{lab} = 149.7, 139.7,$ and 129.7 MeV, where σ_{fus} data were available. The ϵ_{HYRA} for the $^{32}\text{S}+^{138}\text{Ba}$ has been extracted using Eq. (1), and an average value of $13.2\% \pm 1.4\%$ was obtained.

The ϵ_{HYRA} for $^{30}\text{Si}+^{140}\text{Ce}$ system has been evaluated by comparing the angular distribution of both systems. A realistic angular distribution of ERs was generated through the semi-microscopic Monte Carlo simulation code TERS (Transmission Efficiency of Recoil Separator) [41] on an event-by-event basis. Parameters such as position, angle, charge state, and energy were simulated using the code. The PACE4 predicted ERs, which carried more than 1% of the formation cross section, had been simulated. The input parameters corresponding to various ERs, such as the proton, neutron, and α -separation energies, were entered into the TERS code along with incident energy, target thickness, etc. For comparison, the total number of ERs was kept the same during calculations for all the energies. The angular distribution of different ERs was added at each energy according to their PACE4 calculated proportion. Subsequently, the normalized yield was calculated within 9.5° of HYRA's polar acceptance range for the first quadrupole. To get the estimated ϵ_{HYRA} , we assume that the charge state acceptance of HYRA is nearly 100%, and the factor that causes a difference in ϵ_{HYRA} is the angular distribution of the ERs within 9.5° as we had optimized the magnetic field values and gas pressure carefully. The normalized yield within HYRA's polar acceptance was found to be nearly the same for both systems at $E_{lab} = 132.0$ MeV. Therefore, the same transmission efficiency might be assumed for $^{30}\text{Si}+^{140}\text{Ce}$ system. The normalized yield trend

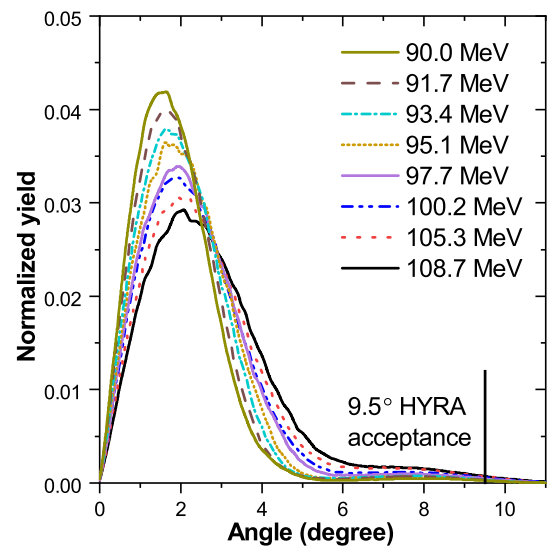


Fig. 3 The normalized yield distribution of the sum of ERs for $^{30}\text{Si}+^{140}\text{Ce}$ reaction at several energies simulated through the Monte Carlo code TERS. For the whole energy range (c.m. frame), the distribution is largely focused inside HYRA for the angular opening of 9.5°

of ERs for $^{30}\text{Si}+^{140}\text{Ce}$ system at different incident energies is shown in Fig. 3.

In order to calculate the ϵ_{HYRA} for different incident energies, the normalized ER yields have been compared and scaled with the ER yield at $E_{lab} = 132.0$ MeV ($E_{c.m.} = 108.7$ MeV) where ϵ_{HYRA} was $13.2\% \pm 1.4\%$. The scaled values of ϵ_{HYRA} vary between 13.2% and 13.3% . The error (Δ) in σ_{fus} is calculated as follows:

$$\sqrt{\left(\frac{1}{\sqrt{Y_{ER}}}\right)^2 + \left(\frac{1}{\sqrt{Y_{mon}}}\right)^2 + \left(\Delta \frac{d\sigma}{d\Omega}\right)_R^2 + (\Delta\Omega_{mon})^2 + (\Delta\epsilon_{HYRA})^2}. \quad (3)$$

3.2 Interpretation using coupled-channel code CCFULL

The measured ER cross section should sum up to the total fusion cross section (σ_{fus}) due to negligible fission contribution in the given experimental energy range. Therefore, the coupled-channel (CC) code CCFULL was employed to decipher the cross section data (Table 1). The quantum-mechanical CC formalism can explain the σ_{fus} by encompassing the effect of couplings to various degrees of freedom of the participating nuclei around the barrier compared to the 1D-BPM predictions. Albeit different forms of nuclear potentials have been put forth in literature, the Woods-Saxon potential with Akyüz-Winther (AW) parameters [42] form the basis of present CCFULL calculations. These parameters are: depth of the nuclear potential (V_0), radius parameter (r_0), and diffuseness parameter (a_0). Considering the sensitivity of parameters [42], V_0 , r_0 , and a_0 were adjusted in CC

Table 1 Measured total fusion cross section (σ_{fus}) for $^{30}\text{Si}+^{140}\text{Ce}$ reaction at different incident energies

$E_{c.m.}$ (MeV)	σ_{fus} (mb)
86.6	0.010 ± 0.002
88.3	0.07 ± 0.013
90.0	0.40 ± 0.07
91.7	2.3 ± 0.4
93.4	7.1 ± 1.2
95.1	20.6 ± 3.4
97.7	75.8 ± 12.4
100.2	135.0 ± 22.1
102.8	194.1 ± 31.7
105.3	264.0 ± 43.1
108.7	337.8 ± 55.2

Table 2 Akyüz–Winther parameters, i.e, depth of the potential V_0 , radius parameter r_0 , and diffuseness parameter a_0 of Woods–Saxon potential used in CCFULL calculations for $^{30}\text{Si}+^{140}\text{Ce}$ reaction. The derived uncoupled barrier parameters have also been provided

Akyüz–Winther parameters		Uncoupled barrier parameters	
V_0 (c.m) (MeV)	82.0	V_B (MeV)	96.89
r_0 (fm)	1.165	R_B (fm)	11.29
a_0 (fm)	0.67	$\hbar\omega$ (MeV)	4.06

calculations to fit the cross section data. It has been made sure that the derived uncoupled barrier parameters, such as the obtained Coulomb barrier height (V_B) and radius (R_B), almost replicate the database values [37]. The parameters are given in Table 2.

The measured cross section shows an enhancement greater than the factor of 10^2 compared to the predictions of 1D-BPM in the sub-barrier region, as shown in Fig. 4a. The CC calculations have been performed to work out the underlying cause by incorporating the couplings to the low-lying inelastic states of the interacting partners into the 1D-BPM. The system has negative ground state Q-values for transfer as indicated in Table 3.

3.2.1 Structural parameters

Comprehending the ground state structure in the $2s-1d$ shell region with clarity remains a challenging issue. Various literature sources report contrasting values of the deformation parameter for ^{30}Si . While Möller et al. report the quadrupole deformation parameter $\beta_2 = -0.236$ [43], the atomic data table of Raman et al. quote $\beta_2 = 0.315$ [44] based upon its intrinsic nuclear quadrupole moment $Q_0 = 0.465$. On the contrary, N. J. Stone [45,46] puts forth the measured quadrupole moment $Q(b)$ of ^{30}Si as -0.05 [45,46], where b represents barn. It indicates a nearly spherical ground state. This $Q(b)$

results in negligible value of β_2 parameter. Predictions based upon mean field theories [47] suggest a probability of ^{30}Si going from prolate to oblate shape via spherical ground state [48]. The target ^{140}Ce has been reported to show zero [43] to small value of β_2 [44], without much disparity, indicating a nearly spherical nucleus exhibiting neutron shell-closure at 82. The deformation parameter has been calculated as follows:

$$\beta_\lambda = \frac{4\pi}{3Z_i R_i^\lambda} \sqrt{\frac{B(E\lambda) \uparrow}{e^2}} \tag{4}$$

$$B(E2) \uparrow = \frac{5}{16\pi} |eQ_0^2|. \tag{5}$$

Where $B(E\lambda)$ is the electric transition probability in e^2b^λ units where λ is the multipolarity, e is the electronic charge, and b represents barn. Z_i and R_i represent the atomic number and nuclear radius of the projectile/target, respectively. The nuclear radius $R_i = R_0 A^{1/3}$, where R_0 is the radius parameter.

We tried different β_2 values of ^{30}Si in the CCFULL calculations along with vibrational couplings and found that $\beta_2^{vib} = 0.315$ closely reproduced our data. The β_2 and β_3 values of both ^{30}Si and ^{140}Ce have been calculated using the formulations of Raman et al. and Kibedi et al., respectively [44,49], as given in Eqs. (4) and (5). The detailed structural parameters of ^{30}Si and ^{140}Ce used in the calculations are presented in Table 4.

3.2.2 Excitation function

Initially, vibrational excitations of the first 2^+ state (1.596 MeV) [50] of the target ^{140}Ce have been included in the calculations (see Fig. 4a). It leads to a minor enhancement in the sub-barrier fusion cross section, possibly due to the too-low excitation energy of the 2^+ state. Including higher phonon states of 2^+ does not cause any noticeable change to the theoretical cross section. CCFULL takes the excitation energy of the n -phonon state as n times that of the single-phonon state [27] in the harmonic oscillator approximation. Thereafter, coupling to the first 3^- state (2.464 MeV) state is included with 2^+ state, which causes significant fusion enhancement in the sub-barrier region. Further addition of phonon states to 3^- does not induce a significant change in cross section. The effect of inelastic excitations is not apparent in the above-barrier region but is clear in the sub-barrier region.

The first excited 2^+ state in ^{30}Si lies at 2.235 MeV and is collective ($\beta_2/\beta_{2sp} = 2.78$ [44]) in nature and hence, will also contribute to the fusion enhancement. By including the coupling to the first 2^+ state, significant sub-barrier fusion cross section enhancement has been witnessed compared to 1D-BPM. Due to the higher excitation energy and β_2 value, the effect of increasing the phonon state of 2^+ level (red dashed line) is remarkable. The measured data is well reproduced

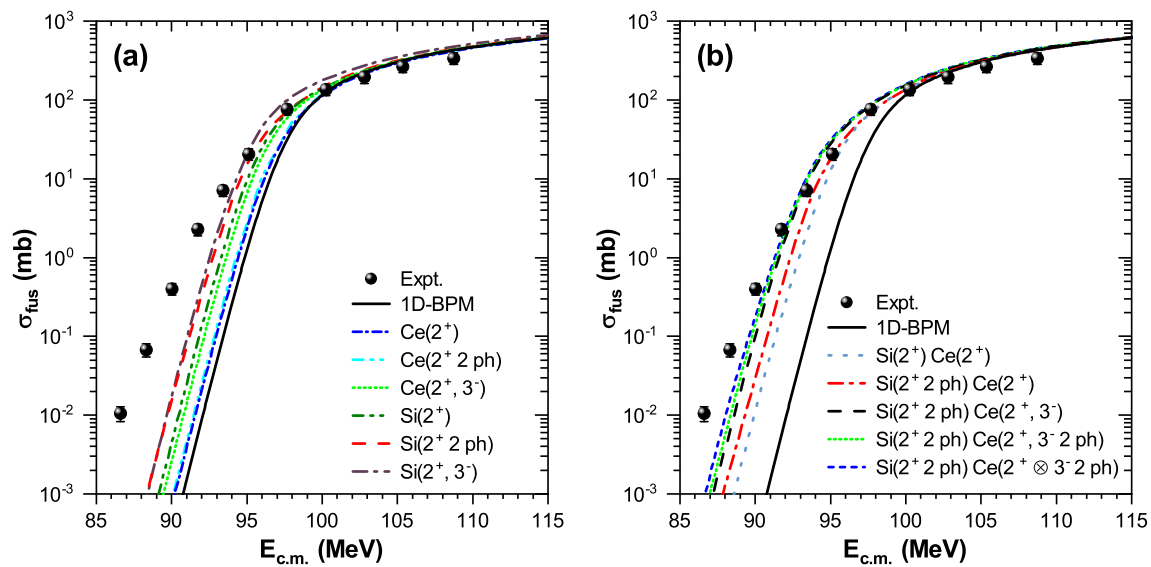


Fig. 4 Comparison of measured fusion cross section of $^{30}\text{Si}+^{140}\text{Ce}$ with CCFULL calculations for 1D-BPM (black solid line) and couplings to collective states (broken lines) in (a) individual projectile and target nuclei, and (b) both projectile and target nuclei (see the text for details)

Table 3 Information of the ground state neutron-transfer Q-values for $^{30}\text{Si}+^{140}\text{Ce}$ system. Q_{+xn} and Q_{-xn} stand for the ground-state Q-value (MeV) for neutron pickup and stripping, respectively [37]

Pickup	Q_{+xn}	Stripping	Q_{-xn}
1n	-2.61	1n	-5.18
2n	-0.86	2n	-6.49
3n	-6.08	3n	-18.52
4n	-6.05	4n	-24.94
5n	-13.53	5n	-39.27
6n	-15.28	6n	-47.62

Table 4 Nuclear structure parameters of ^{30}Si and ^{140}Ce nuclei including multipolarity (λ); spin-parity (J^π); excitation energy (E^*); and deformation (β_λ) incorporated in CCFULL calculations. The β_2 and β_3 values have been calculated from Eq. (4) using the systematics of Raman et al. and Kibedi et al. [44,49], respectively. The energies of various levels have been taken from the ref. [50]

Nucleus	λ	J^π	E^*	β_λ
^{30}Si	2	2^+	2.235	0.315
	3	3^-	5.487	0.275
^{140}Ce	2	2^+	1.596	0.1015
	3	3^-	2.464	0.127

down to 95 MeV. The addition of vibrational 3^- state overpredicts the near-barrier fusion cross section. At the same time, the sub-barrier region data also remains largely unexplained. The effect of couplings on the projectile's states is more robust than the target's states, which might be due to the large quadrupole and octupole deformation, and relatively high energy of the low-lying inelastic states of the projectile.

The combined effect of channel couplings of both the colliding partners is shown in Fig 4(b). At first, ^{30}Si (2^+) and ^{140}Ce (2^+) states are included, which explains the data from the above barrier to the near barrier region. One may see that ^{30}Si (2^+) up to two phonon states along with ^{140}Ce (2^+) results in an improved fitting of data down to 93 MeV (red dash-dotted line). However, the four lowermost energy data are far from the theoretical calculation. One-by-one inclusion of the 3^- state of Ce with one and two phonons results in improved data reproduction in the lower-energy region. Eventually, a combination of all the mentioned states, i.e., mutual excitations (\otimes) among the (2^+) and (3^- 2 ph) states of ^{140}Ce is considered (blue dashed line). The mutual excitations involve the combinations (2^+ 0 ph, 3^- 0 ph), (2^+ 0 ph, 3^- 1 ph), (2^+ 0 ph, 3^- 2 ph), (2^+ 1 ph, 3^- 0 ph), (2^+ 1 ph, 3^- 1 ph), and (2^+ 1 ph, 3^- 2 ph). Though the calculation enhances the sub-barrier fusion cross section and becomes closer to the lower energy data, it compromises the explanation of near-barrier data simultaneously. One can learn that not a single type of channel-coupling can fully predict the experimental cross sections of $^{30}\text{Si}+^{140}\text{Ce}$ system. Additionally, when higher-order couplings are taken, the program does not effectively handle all possible mutual excitations among the energy and phonon states of the projectile and target. Nevertheless, it must be pointed out that the collective structural behavior of nuclei is more plausible than the single particle behavior.

The effect of the radius parameter (R_0) of the projectile and target on σ_{fus} calculations has been seen in CCFULL, which incorporates the radius of individual projectile and target as $R_i = R_0 A_i^{1/3}$ fm. Inquiries on the coupled-channel calculations reveal the appropriateness of $R_0 = 1.20$ fm for

explaining the fusion data compared to other values of R_0 , such as 1.15 and 1.10 fm. Consequently, $R_0 = 1.20$ fm was chosen for the calculations.

3.3 Fusion barrier distribution

The peculiarities of the sub-barrier fusion phenomenon in nuclear collisions are implied through the barrier distribution (BD) plot. It has been seen that the couplings to inelastic excitations in CCFULL have partially explained the measured σ_{fus} for the $^{30}\text{Si}+^{140}\text{Ce}$ system. As a matter of fact, these couplings split the single barrier into multiple components of various strengths, making the sub-barrier fusion more probable; and to observe the nature and impact of couplings involved in sub-barrier fusion, the analysis of BD is a fundamental requisite [5,30]. The fusion BD has been derived from the measured fusion excitation function through Eq. (6).

$$D_{fus}(E) = \frac{d^2(E\sigma_{fus})}{dE^2} \quad (6)$$

The double-derivative of the energy-weighted σ_{fus} with respect to incident energy has been found by the three-point difference formula, a procedure explained in a detailed review by Dasgupta et al. [5]. The BD for $^{30}\text{Si}+^{140}\text{Ce}$ reaction has been presented in Fig. 5, where the 1D-BPM predicted single peak manifests the uncoupled barrier. However, the measured fusion BD differs strikingly, broadening and splitting into two major peaks. The uncertainty in the BD increases with $\Delta\sigma_{fus}$ and energy, which makes it unclear or poorly defined at higher energies. To understand the fusion BD meaningfully, only the statistical uncertainties have been considered in measuring the counts, while the systematic uncertainties have been neglected. This approach was followed earlier in Refs. [51,52]. The energy interval in the below-barrier region is ≈ 2 MeV, while it is ≈ 3 MeV above the barrier.

The CC calculations have been performed with different projectile-target low-lying inelastic excitations to account for the measured trend of BD. Initially, the effect of nuclear surface vibrations in the target has been considered, with coupling to 2^+ state. It closely reproduces the measured BD up to 100 MeV. The higher-energy (above the Coulomb barrier) side of the BD has a smaller peak, which might be a consequence of couplings to the projectile's excited states. Earlier, the effect of couplings on the ^{30}Si was found to be more robust than the vibration couplings in ^{140}Ce (see Fig. 4). Considering $^{30}\text{Si}(2^+)$ in the CC calculations, the BD somewhat resembles the trend of above-barrier measured data but does not reproduce it reasonably. This improves slightly after incorporating $\text{Ce}(2^+, 3^- 2\text{ ph})$; however, the explanation of the lower energy side gets compromised. The further intervention of couplings to the states of ^{30}Si and ^{140}Ce compli-

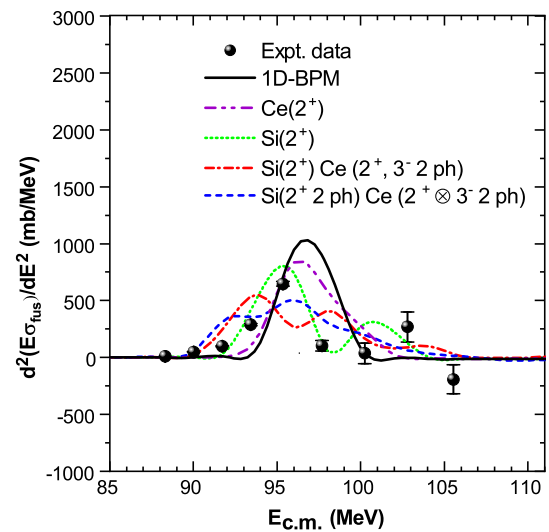


Fig. 5 Illustration of fusion barrier distribution (BD) for $^{30}\text{Si} + ^{140}\text{Ce}$ system. The CCFULL predicted BD using 1D-BPM and couplings to inelastic excitations have also been showcased. The systematic uncertainties have been subtracted from the total cross section error (see the text for details)

cates the BD and fails to justify the experimental data. It is noticeable that the set of coupling parameters explaining the BD is somewhat simpler than those explaining the σ_{fus} in Fig. 4.

3.4 Study of the entrance channel effect

To investigate the multidimensional effect of the structure of the participating nuclei on σ_{fus} in the near and sub-barrier region, the σ_{fus} of the $^{30}\text{Si}+^{140}\text{Ce}$ system has been compared with those reported in the literature. The comparison has been made on a reduced scale of cross section and energy as given below:

$$\sigma_{red} = 2\sigma_{fus} E_{c.m.} / R_B^2 \hbar\omega \quad (7)$$

$$E_{red} = (E_{c.m.} - V_B) / \hbar\omega. \quad (8)$$

Introducing the dimensionless variables, σ_{red} and E_{red} [53], eliminates the variability in V_B , R_B , and barrier curvature $\hbar\omega$ among different systems due to their charge and geometric sizes. Therefore, one can understand the role of different degrees of freedom of the colliding nuclei in the sub-barrier fusion unambiguously for systems with varying entrance channel mass asymmetry [53]. The energies of the lowest 2^+ and 3^- levels, β_2 have been provided in Tables 5 and 6. To maintain the uniformity, Woods-Saxon potential parameters (V_B , R_B , and $\hbar\omega$) for all systems have been extracted through the CCFULL code using the Akyüz-Winther parameters (V_0 , r_0 , and a_0) provided in Ref. [57].

The present study has been compared with the results of some nearby systems (Fig. 6a) exhibiting structural deforma-

Table 5 Information of projectile and target nuclei in different reactions. The value of energy levels $E(2^+)$ and $E(3^-)$ (in MeV) have been taken from the Ref. [50], while the quadrupole deformation parameter (β_2) is taken from the table of S. Raman et al. [44]. The transfer Q_{+xn} [37] stands for the ground state Q-value (in MeV) for neutron pickup by the projectile from the target

	$^{28}\text{Si}+^{90}\text{Zr}$ [18]	$^{28}\text{Si}+^{116}\text{Sn}$ [14]	$^{30}\text{Si}+^{140}\text{Ce}$ [Present]	$^{32}\text{S}+^{112}\text{Sn}$ [8]	$^{30}\text{Si}+^{156}\text{Gd}$ [19]
$E(2^+)$	1.779 2.186	1.779 1.293	2.235 1.596	2.230 1.256	2.235 0.088
$E(3^-)$	6.878 2.747	6.878 2.266	5.487 2.464	5.006 2.354	5.487 1.276
β_2	0.407 0.089	0.407 0.112	0.315 0.102	0.312 0.123	0.315 0.338
Q_{+2n}	-2.20	1.97	-0.86	1.10	0.81

Table 6 Information of projectile and target nuclei in different reactions. The value of energy levels $E(2^+)$ and $E(3^-)$ (in MeV) have been taken from the ref. [50], while the quadrupole deformation parameter (β_2) is taken from the table of S. Raman et al. [44]. The transfer Q_{+xn} [37] stands for the ground-state Q-value (in MeV) for neutron pickup by the projectile from the target

	$^{28}\text{Si}+^{124}\text{Sn}$ [14]	$^{32}\text{S}+^{120}\text{Sn}$ [8]	$^{40}\text{Ca}+^{124}\text{Sn}$ [54]	$^{28}\text{Si}+^{154}\text{Sm}$ [55]	$^{32}\text{S}+^{154}\text{Sm}$ [56]
$E(2^+)$	1.779 1.131	2.230 1.171	3.904 1.131	1.779 0.082	2.230 0.082
$E(3^-)$	6.878 2.602	5.006 2.400	3.736 2.602	6.878 1.012	5.006 1.012
β_2	0.407 0.095	0.312 0.108	0.123 0.095	0.407 0.341	0.312 0.341
Q_{+1n}	-0.02	-0.46	-0.13	0.51	0.67
Q_{+2n}	4.65	4.47	5.41	5.25	6.22
Q_{+3n}	2.42	2.13	4.52	3.58	4.95
Q_{+4n}	5.45	5.08	9.49	7.18	9.24
Q_{+5n}	0.85	-0.18	7.80	3.70	5.56
Q_{+6n}	1.88	0.30	11.71	5.34	7.73

tion but negative Q-values for n -transfer. Albeit some systems have a small positive Q-value for $2n$ -pickup by the projectile from the target (Table 5), no significant effect was reported due to the $2n$ -transfer in the sub-barrier region. The interplay of quadrupole deformation β_2 and $2n$ -transfer is suggested by Sargsyan et al. based on β_2 value before and after the transfer [58].

The deformation plays a compassionate role in the sub-barrier fusion enhancement, which is remarkably visible for $^{30}\text{Si}+^{156}\text{Gd}$ system [19]. The enhancement is comparable for the $^{32}\text{S}+^{112}\text{Sn}$ [8], $^{28}\text{Si}+^{116}\text{Sn}$ [14], and $^{30}\text{Si}+^{140}\text{Ce}$ system (present). The slope of fusion EF is also similar due to the proton/neutron magic number of the targets as earlier observed by Kalkal et al. [18]. The fusion in case of $^{28}\text{Si}+^{90}\text{Zr}$ (neutron magic) [18] system goes down even when β_2 is higher for ^{28}Si . This is probably because of the lower value of the charge product $Z_P Z_T$ compared to other systems. Sargsyan et al. [58, 59] also pointed out that the effect of the quadrupole deformation increases with $Z_P Z_T$.

A comparison has been made again with the results of some nearby systems having mostly positive Q -values for n -pickup up to $6n$ (Table 6) or more (Fig. 6b). For $^{32}\text{S}+^{154}\text{Sm}$ [56] and $^{28}\text{Si}+^{154}\text{Sm}$ [55], the β_2 values are large and comparable, and the effect on fusion is quite evident in the sub-barrier region. $^{40}\text{Ca}+^{124}\text{Sn}$ [54], $^{32}\text{S}+^{120}\text{Sn}$ [8], $^{28}\text{Si}+^{124}\text{Sn}$ [14] show similar slopes for the fusion EF that might be due

to doubly magic (^{40}Ca) and semimagic ($^{124,120}\text{Sn}$) nature of the nuclei involved [18]. $^{40}\text{Ca}+^{124}\text{Sn}$ shows significantly greater value of the fusion cross section even while having lower β_2 values. The nature of 2^+ state ($\beta_2/\beta_{2sp}=1.55$) [44] is hardly collective in this case. The high cross section might be due to the (i) high magnitude of positive Q-values compared to the other two systems or/and (ii) more pronounced effect of neutron transfer in the case of more spherical magic or nearly magic nuclei [60]. The present system has all negative Q-values for n -transfer and shows lower sub-barrier fusion compared to similarly deformed $^{32}\text{S}+^{120}\text{Sn}$ system, exhibiting PQNT.

It is clear from the above comparisons that several factors simultaneously decide the effect of the entrance channel on sub-barrier fusion. More studies are required to account for the unambiguous role of each factor in driving the reaction process.

4 Conclusion

We report the total fusion measurement of $^{30}\text{Si}+^{140}\text{Ce}$ reaction in a wide energy range ($E_{c.m.} = 86.6-108.7$ MeV), which spans 11% below to 13% above the Coulomb barrier. The fusion cross section has been seen enhanced by several orders of magnitude in the sub-barrier energy region

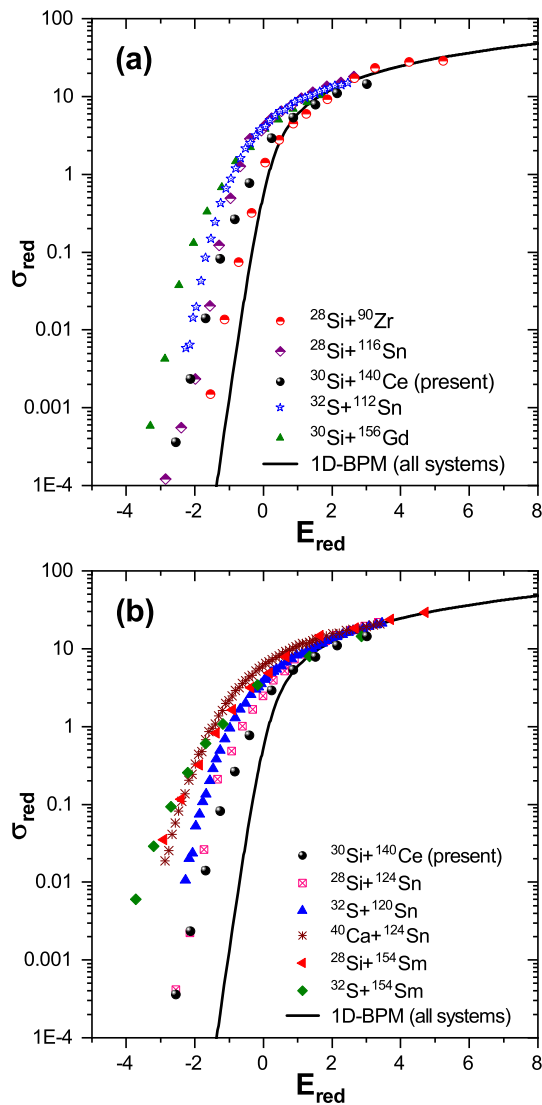


Fig. 6 Excitation functions on a reduced scale of cross section $\sigma_{red} = 2\sigma_{fus} E_{c.m.}/R_B^2 \hbar\omega$ and incident energy $E_{red} = (E_{c.m.} - V_B)/\hbar\omega$ for the reactions in nearby mass region having (a) all negative or small positive Q-values corresponding to $2n$ -pickup by the projectile from the target and (b) positive Q-values up to $6n$ -pickup or more (see the text for details)

compared to the 1D-BPM predictions. The total fusion cross section enhancement has been understood by including collective excitations of the low-lying states of interacting nuclei in the coupled-channel code CCFULL. The projectile ^{30}Si and target ^{140}Ce have been considered as vibrators in the CCFULL calculations. The calculations have met only partial success as the measured fusion cross sections are not explained over the whole energy range through one particular type of couplings. The near-barrier data have been well explained by incorporating the coupling to 2^+ state of ^{30}Si with two phonon excitation and 2^+ state of ^{140}Ce . Concurrently, the sub-barrier energy data has been partially explained by addi-

tionally incorporating the two phonon state of 3^- in ^{140}Ce . Data reproduction improves further by including the effect of all mutual excitations among these states of the target nucleus. It is seen that there is a need for improved treatment of mutual excitations among the inelastic states in the CCFULL program for higher-order couplings. It merits mention that the role of collective degrees of freedom is quite adequate, and the effect of structural deformation in ^{30}Si has been found to be quite prominent in sub-barrier fusion enhancement. To understand the channel-coupling effect more intricately, the $^{30}\text{Si}+^{140}\text{Ce}$ reaction has been compared with several other reactions in the nearby mass region on a reduced scale. The effect of deformation in the nuclei is found to be more vigorous than the transfer-channel couplings in the sub-barrier region. More reaction data and systematic comparisons can effectively substantiate the explanations of the sub-barrier fusion enhancement phenomenon.

Acknowledgements The authors sincerely thank the Pelletron staff of the Inter-University Accelerator Centre (IUAC) for their cooperation and invaluable help during the experiment. Student research fellowships from the MHRD, DST-INSPIRE (IF180078), and UGC, Government of India, are gratefully acknowledged.

Data Availability Statement This manuscript has no associated data. [Author's comment: Datasets were generated and analysed during the current study and the data have been provided in Table 1].

Code Availability Statement This manuscript has no associated code/software. [Author's comment: We do not have any code/software to share along with present data].

References

1. M. Beckerman, J. Ball, H. Enge, M. Salomaa, A. Sperduto, S. Gazes, A. Di Rienzo, J.D. Molitoris, Phys. Rev. C **23**, 1581 (1981)
2. R.G. Stokstad, Y. Risen, S. Kaplanis, D. Pelte, U. Smilansky, I. Tserruya, Phys. Rev. Lett. **41**, 465 (1978)
3. R.G. Stokstad, Y. Eisen, S. Kaplanis, D. Pelte, U. Smilansky, I. Tserruya, Phys. Rev. C **21**, 2427 (1980)
4. M. Beckerman, Phys. Rep. **129**, 145 (1985)
5. M. Dasgupta, D.J. Hinde, N. Rowley, A.M. Stefanini, Annu. Rev. Nucl. Part. C **48**, 401 (1998)
6. C.H. Dasso, S. Landowne, A. Winther, Nucl. Phys. A **405**, 381 (1983)
7. M. Beckerman, Rep. Prog. Phys. **51**, 1047 (1988)
8. V. Tripathi, L.T. Baby, J.J. Das, P. Sugathan, N. Madhavan, A.K. Sinha, P.V.M. Rao, S.K. Hui, R. Singh, K. Hagino, Phys. Rev. C **65**, 014614 (2001)
9. A.M. Stefanini, F. Scarlassara, S. Beghini, G. Montagnoli, R. Silvestri, M. Trotta, B.R. Behera, L. Corradi, E. Fioretto, A. Gadea et al., Phys. Rev. C **73**, 034606 (2006)
10. A.M. Stefanini, B.R. Behera, S. Beghini, L. Corradi, E. Fioretto, A. Gadea, G. Montagnoli, N. Rowley, F. Scarlassara, S. Szilner, Phys. Rev. C **76**, 014610 (2007)
11. H. Esbensen, G. Montagnoli, A.M. Stefanini, Phys. Rev. C **93**, 034609 (2016)
12. G. Pollarolo, A. Winther, Phys. Rev. C **62**, 054611 (2000)

13. H. Timmers, L. Corradi, A.M. Stefanini, D. Ackermann, J.H. He, S. Beghini, G. Montagnoli, F. Scarlassara, G.F. Segato, N. Rowley, *Phys. Lett. B* **399**, 35 (1997)
14. A. Rani, S. Mandal, K. Chakraborty, R. Gupta, C.V. Ahmad, A. Parihari, D. Vishwakarma, P. Khandelwal, P.S. Rawat, P. Sherpa et al., *Phys. Rev. C* **106**, 064606 (2022)
15. A. Chauhan, R. Prajapat, G. Sarkar, M. Maiti, R. Kumar, Gonika Malvika, J. Gehlot, S. Nath, A. Parihari et al., *Phys. Rev. C* **102**, 064606 (2020)
16. R.N. Sahoo, M. Kaushik, A. Sood, P. Kumar, A. Sharma, S. Thakur, P.P. Singh, P.K. Raina, Md.M. Shaikh, R. Biswas et al., *Phys. Rev. C* **99**, 024607 (2019)
17. R.N. Sahoo, M. Kaushik, A. Sood, A. Sharma, S. Thakur, P. Kumar, Md.M. Shaikh, R. Biswas, A. Yadav, M.K. Sharma et al., *Phys. Rev. C* **102**, 024615 (2020)
18. S. Kalkal, S. Mandal, N. Madhavan, E. Prasad, S. Verma, A. Jhingan, R. Sandal, S. Nath, J. Gehlot, B.R. Behera et al., *Phys. Rev. C* **81**, 044610 (2010)
19. R. Prajapat, M. Maiti, R. Kumar, M. Sagwal, Gonika, C. Kumar, R. Biswas, S. Nath, J. Gehlot, N. Madhavan, *Phys. Rev. C* **105**, 064612 (2022)
20. P.K. Rath, S. Santra, N.L. Singh, B.K. Nayak, K. Mahata, R. Palit, K. Ramachandran, S.K. Pandit, A. Parihari, A. Pal et al., *Phys. Rev. C* **88**, 044617 (2013)
21. E. Martínez-Quiroz, E.F. Aguilera, J.J. Kolata, M. Zahar, *Phys. Rev. C* **63**, 054611 (2001)
22. J.J. Vega, E.F. Aguilera, G. Murillo, J.J. Kolata, A. Morsad, X.J. Kong, *Phys. Rev. C* **42**, 947 (1990)
23. C.L. Jiang, K.E. Rehm, B.B. Back, H. Esbensen, R.V.F. Janssens, A.M. Stefanini, G. Montagnoli, *Phys. Rev. C* **89**, 051603(R) (2014)
24. R. Prajapat, M. Maiti, R. Kumar, M. Sagwal, C. Kumar, Gonika, R. Biswas, S. Nath, J. Gehlot, N. Madhavan, *Phys. Rev. C* **107**, 064616 (2023)
25. P.H. Stelson, *Phys. Lett. B* **205**, 190 (1988)
26. G. Montagnoli, S. Beghini, F. Scarlassara, A.M. Stefanini, L. Corradi, C.J. Lin, G. Pollarolo, A. Winther, *Eur. Phys. J. A* **15**, 351 (2002)
27. K. Hagino, N. Rowley, A.T. Kruppa, *Comp. Phys. Comm.* **123**, 143 (1999)
28. V.I. Zagrebaev, V.V. Samarin, W. Greiner, *Phys. Rev. C* **75**, 035809 (2007)
29. B.B. Back, H. Esbensen, C.L. Jiang, K.E. Rehm, *Rev. Mod. Phys.* **86**, 317 (2014)
30. N. Rowley, G.R. Satchler, P.H. Stelson, *Phys. Lett. B* **254**, 25 (1991)
31. B.K. Nayak, R.K. Choudhury, A. Saxena, P.K. Sahu, R.G. Thomas, D.C. Biswas, B.V. John, E.T. Mirgule, Y.K. Gupta, M. Bhike et al., *Phys. Rev. C* **75**, 054615 (2007)
32. R. Biswas, S.R. Abhilash, H. Gupta, G.R. Umapathy, A. Dawar, S. Nath, *Vacuum*. **188**, 110159 (2021)
33. N. Madhavan, S. Nath, T. Varughese, J. Gehlot, A. Jhingan, P. Sugathan, A.K. Sinha, R. Singh, K.M. Varier, M.C. Radhakrishna et al., *Pramana -J. Phys.* **75**, 317 (2010)
34. S. Muralithar, N. Madhavan, P. Sugathan, R.P. Singh, A. Jhingan, R. Kumar, S. Nath, K.S. Golda, J. Gehlot, *Eur. Phys. J. A* **58**, 250 (2022)
35. S. Nath, A Monte Carlo code to model ion transport in dilute gas medium (unpublished)
36. J.F. Ziegler, M.D. Ziegler, J.P. Biersack, *Nucl. Instrum. Methods Phys. Res. B* **268**, 1818 (2010)
37. <http://nrv.jinr.ru/nrv/webnrv/qcalc/>
38. <http://www.iuac.res.in/NIAS/?url=NiasMARS/> Accessed on 18 june 2024
39. A. Gavron, *Phys. Rev. C* **21**, 230 (1980)
40. S. Gil, F. Hasenbalg, E. Testoni, D. Abriola, M.C. Berisso, M. di Tada, A. Etchegoyen, J.O. Fernandez Niello, A.J. Pacheco, *Phys. Rev. C* **51**, 1336 (1995)
41. S. Nath, *Comput. Phys. Commun.* **180**, 2392 (2009)
42. R.A. Broglia, A. Winther, *Heavy Ion Reactions* (Benjamin Cummings, San Francisco, 1981)
43. P. Möller, A.J. Sierk, T. Ichikawa, H. Sagawa, *At. Data Nucl. Data Tables* **109–110**, 1 (2016)
44. S. Raman, C.W. Nestor Jr., P. Tikkanen, *At. Data Nucl. Data Tables* **78**, 1 (2001)
45. N.J. Stone, *At. Data Nucl. Data Tables* **90**, 75 (2005)
46. N.J. Stone, *At. Data Nucl. Data Tables* **111–112**, 1 (2016)
47. H. Mei, K. Hagino, J.M. Yao, T. Motoba, *Phys. Rev. C* **97**, 064318 (2018)
48. Y.K. Gupta, G.K. Prajapati, B. Maheshwari, A.K. Jain, K. Hagino, B.N. Joshi, V.B. Katariya, D. Patel, U. Garg, A. Pal et al., *Proceedings of the DAE Symp. on Nucl. Phys.* **67**, 421 (2023)
49. T. Kibedi, R.H. Spear, *At. Data Nucl. Data Tables* **80**, 35 (2002)
50. <https://www.nndc.bnl.gov/nudat3/> Accessed on 18 june 2024
51. A.M. Stefanini, D. Ackermann, L. Corradi, D.R. Napoli, C. Petrace, P. Spolaore, P. Bednarczyk, H.Q. Zhang, *Phys. Rev. Lett.* **74**, 864 (1995)
52. J.R. Leigh, M. Dasgupta, D.J. Hinde, J.C. Mein, C.R. Morton, R.C. Lemmon, J.P. Lestone, J.O. Newton, H. Timmers, J.X. Wei, *Phys. Rev. C* **52**, 3151 (1995)
53. N.V.S.V. Prasad, A.M. Vinodkumar, A.K. Sinha, K.M. Varier, D.L. Sastry, N. Madhavan, R. Sugathan, D.O. Kataria, J.J. Das, *Nucl. Phys. A* **603**, 176 (1996)
54. F. Scarlassara, S. Beghini, G. Montagnoli, G.F. Segato, D. Ackermann, L. Corradi, C.J. Lin, A.M. Stefanini, L.F. Zheng, *Nucl. Phys. A* **672**, 99 (2000)
55. S. Gil, D. Abriola, D.E. DiGregorio, M. di Tada, M. Elgue, A. Etchegoyen, M.C. Etchegoyen, J.F. Niello, A.M.J. Ferrero, A.O. Macchiavelli et al., *Phys. Rev. Lett.* **65**, 3100 (1990)
56. P.R.S. Gomes, I.C. Charret, R. Wanis, G.M. Sigaud, V.R. Vanin, R.L. Neto, D. Abriola, O.A. Capurro, D.E. DiGregorio et al., *Phys. Rev. C* **49**, 245 (1994)
57. <http://nrv.jinr.ru/nrv/webnrv/fusion/> Accessed on 18 june 2024
58. V.V. Sargsyan, G.G. Adamian, N.V. Antonenko, W. Scheid, H.Q. Zhang, *Phys. Rev. C* **85**, 024616 (2012)
59. V.V. Sargsyan, G.G. Adamian, N.V. Antonenko, W. Scheid, C.J. Lin, H.Q. Zhang, *Phys. Rev. C* **85**, 037602 (2012)
60. V.A. Rachkov, A.V. Karpov, A.S. Denikin, V.I. Zagrebaev, *Phys. Rev. C* **90**, 014614 (2014)

Springer Nature or its licensor (e.g. a society or other partner) holds exclusive rights to this article under a publishing agreement with the author(s) or other rightsholder(s); author self-archiving of the accepted manuscript version of this article is solely governed by the terms of such publishing agreement and applicable law.